Mechanisms of Global Warming Impacts on Robustness of Tropical Precipitation Asymmetry

Pei-Hua Tan

Department of History and Geography, National Chiayi University, Chiayi, Taiwan

Chia Chou

Research Center for Environmental Changes, Academia Sinica, and Department of Atmospheric Sciences, National Taiwan University, Taipei, Taiwan

Jien-Yi Tu

Department of Atmospheric Sciences, Chinese Culture University, Taipei, Taiwan

ABSTRACT

Hemispherically and temporally asymmetric tropical precipitation responses to global warming are evaluated in 13 different coupled atmosphere–ocean climate model simulations. In the late boreal summer, hemispherical averages of the tropical precipitation anomalies from the multimodel ensemble show a strong positive trend in the Northern Hemisphere and a weak negative trend in the Southern Hemisphere. In the late austral summer, on the other hand, the trends are reversed. This implies that the summer hemisphere becomes wetter and the winter hemisphere becomes a little drier in the tropics. Thus, the seasonal range of tropical precipitation, differences between wet and dry seasons, is increased. Zonal averages of the precipitation anomalies from the multimodel ensemble also reveal a meridional movement, which basically follows the seasonal migration of the main convection zone. Similar asymmetric features can be found in all 13 climate model simulations used in this study. Based on the moisture budget analysis, the vertical moisture advection associated with mean circulation is the main contribution for the robustness of the asymmetric distribution of the tropical precipitation anomalies. Under global warming, tropospheric water vapor increases as the temperature rises and most enhanced water vapor is in the lower troposphere. The ascending motion of the Hadley circulation then transports more water vapor upward, that is, anomalous moisture convergence, and enhances precipitation over the main convection zones. On the other hand, the thermodynamic effect associated with the descending motion of the Hadley circulation, that is, anomalous moisture divergence, reduces the precipitation over the descending regions.

1. Introduction

A significant warming trend of globally averaged surface temperature has been found in the past few decades, which is mainly attributed to anthropogenic forcing of greenhouse gases (e.g., Santer et al. 1996; Tett et al. 1999; Mitchell et al. 2001; Jones and Moberg 2003; Tett et al. 2002; Karl and Trenberth 2003; Trenberth et al. 2007). Similar to surface temperature, the tropospheric temperature also increases with time (Fu et al. 2004; Trenberth et al. 2007). For the future projection of climate models to the end of the twenty-first century, the warming becomes much stronger and can be found everywhere, with a different amplitude on a regional scale (e.g., Senior and Mitchell 2000; Cubasch et al. 2001; Meehl et al. 2005; Santer et al. 2005; Johns et al. 2006; Stott et al. 2006; Meehl et al. 2007). This warming trend induced by the anthropogenic forcing is consistent among climate model projections (e.g., Cubasch et al. 2001; Meehl et al. 2007).

In contrast to surface temperature and tropospheric temperature, precipitation changes of climate model simulations reveal a much more complicated pattern, particularly on a regional basis. On a global scale, most model simulations show a positive trend of global-mean

Corresponding author address: Chia Chou, Research Center for Environmental Changes, Academia Sinica, P.O. Box 1-48, Taipei 11529, Taiwan.
E-mail: chiachou@rcec.sinica.edu.tw

precipitation in the future, but this trend has not been found in observations (Allen and Ingram 2002). On a regional scale, projected precipitation changes have great differences in many climate models (e.g., Roeckner et al. 1999; Boer et al. 2000; Meehl et al. 2000; Dai et al. 2001; Williams et al. 2001; Allen and Ingram 2002; Douville et al. 2002; Neelin et al. 2006; Meehl et al. 2007). Disagreement is found not only among climate models, but also between climate models and observations (e.g., Allan and Soden 2007; Trenberth and Dai 2007; Wentz et al. 2007; Zhang et al. 2007). This implies that precipitation changes have complex and distinct behaviors among different regions. A possible reason for the precipitation disagreement among models might be complicated physical processes, such as the hydrological cycle (Allen and Ingram 2002) and the interaction between large-scale dynamics and tropical convection (e.g., Chiang and Sobel 2002; Neelin et al. 2003).

To explain regional precipitation changes, several mechanisms have been proposed (e.g., Chou and Neelin 2004; Chou et al. 2006). On one hand, as the tropospheric relative humidity varies very little (Dai 2006), more column-integrated vapor occurs in convective than in nonconvective regions for each unit of temperature increase, based on the Clausius–Clapeyron equation (Held and Soden 2006). On the other hand, since the atmosphere tends to self-adjust into a stable state via a convective process, when a warmer climate is formed, the atmospheric boundary layer (ABL) moisture in convective regions increases under convective quasi equilibrium (QE). However, this QE mediation does not occur in nonconvective regions (Neelin and Su 2005). Both aforementioned mechanisms create the spatial gradient of ABL moisture anomalies between convective and nonconvective regions. Consequently, the converged inflow in the lower troposphere transports relatively drier air from nonconvective regions to convective regions. This dry advection reduces precipitation in the margin of convective regions, owing to its inability to match the higher required "convective ante," which has been termed the upped-ante mechanism (Neelin et al. 2003; Chou and Neelin 2004). In convective regions, the increase of low-level moisture reduces the effective moist stability and then enhances convection and rainfall, which is the anomalous gross moist stability (M') mechanism or the rich-get-richer mechanism (Chou and Neelin 2004).

Despite great uncertainty in regional precipitation changes, Neelin et al. (2006) examined model simulations and observations to find similarities for tropical droughts over margins of convective regions. Their results show agreement on regional precipitation, especially over Central America and the Caribbean Sea during summer. Other consistent features, such as robust responses of the global hydrological cycle (Held and Soden 2006) and asymmetric responses of tropical precipitation changes between hemispheres (Chou et al. 2007), can also be found from climate model simulations. These consistent features are all associated with the increase of water vapor in the lower troposphere. The aim of this study is to examine what mechanisms control asymmetric responses of tropical precipitation changes between hemispheres and why this asymmetry is in good agreement among different coupled atmosphere–ocean climate models (CGCMs). Model simulations used in this study are presented in section 2. Asymmetry of tropical precipitation changes is discussed in section 3. Diagnosis of the moisture budget and analysis of robust responses of the tropical precipitation asymmetry are given, respectively, in sections 4 and 5, followed by conclusions.

2. The data

The CGCM simulations from the World Climate Research Programme's (WCRP's) Coupled Model Intercomparison Project phase 3 (CMIP3) multimodel dataset for the Fourth Assessment Report (AR4) of the Intergovernmental Panel on Climate Change (IPCC) are used to investigate mechanisms governing asymmetry of tropical precipitation changes under global warming. The 13 models (and sponsoring institution or agency) utilized in this study are listed in Table 1. Monthly variables from the 20C3M simulations for the period from 1860 to 2000 and the Special Report on Emissions Scenarios (SRES) A2 global warming scenario for the period from 2001 to 2100, such as precipitation, specific humidity, surface temperature, air temperature, zonal and meridional wind components, and pressure velocity, are analyzed. The A2 scenario is the warmest scenario in IPCC, warmer than the A1B scenario that is commonly used. There is likely to be some dependence on the emission scenario, which will decrease as time progresses. By the end of the twenty-first century, this dependence should become verylittle. Current climate is the average over the period 1961–90. An anomaly is obtained from the averages in years 2070–99 minus the averages in years 1961–90. One realization for each of the 13 models is examined.

Considering moisture budget analysis, the 13 models (See Table 1) are chosen based on the completeness of datasets at the beginning of the study. However, an evaporation ensemble is computed only from 11 models, excluding models GFDL CM2.1 and CCSR3.2M, owing to a lack of such data outputs. For a similar reason, most terms in the moist static energy are calcu-

TABLE 1. List of the IPCC AR4 CGCM models used for simulations in this study.

Model acronym	Description
CCCMA3.1 _T47	Canadian Centre for Climate Modeling and Analysis (CCCMA) CGCM version 3.1 Model (T47)
CNRM-CM3	Meteo France Centre National de Recherches Météorologiques Coupled Global Climate Model, France, version 3
IPSL CM4.1	L'Institut Pierre-Simon Laplace (IPSL) Coupled Model, version 4.1
GFDL CM2.0	NOAA Geophysical Fluid Dynamics Laboratory, Model CM2.0
GFDL CM2.1	NOAA Geophysical Fluid Dynamics Laboratory (GFDL) Climate Model version 2.1
GISS-ER	NASA Goddard Institute for Space Studies Model E-R
CCSR3.2_M	CCSR Model for Interdisciplinary Research on Climate 3.2, medium-resolution version, Model 32M
MRI CGCM2.3.2	Japan Meteorological Research Institute (MRI) Coupled General Circulation Model, version 2.3.2a
MPI ECHAM5	Max Planck Institute for Meteorology, Germany
NCAR CCSM3	National Center for Atmospheric Research (NCAR) Community Climate System Model, version 3
NCAR PCM1	NCAR Parallel Climate Model (version 1)
INM CM3.0	Institute of Numerical Mathematics Coupled Model, Russia, version 3.0
UKMO HadGEM1	Met Office (UKMO) Hadley Centre Global Environmental Model version 1

lated from 11 models, excluding models ISPL CM4.1 and GISS-ER. An ensemble of net energy into the atmospheric column (F^{net}) is calculated only with seven models: the CCCMA3.1_T47, CNRM-CM3, MRI CGCM2.3.2, MPI ECHAM5, NCAR CCSM3, INM CM3.0), and the UKMO HadGEM1. The moist static energy budget associated with F^{net} does not vary too much even though the model number is reduced from 11 to 7. The 13 models have different horizontal resolutions, so model simulations are interpolated into a uniform grid size, a horizontal resolution of 2.5° latitude × 3.75° longitude, giving 73 × 96 grid points in total. In the vertical, there are 12 unevenly spaced levels extending to 100 hPa in height. We note that interpolation of datasets to a common grid may smooth out some of the extreme precipitation. However, most results are presented either by hemispherical averages or by zonal averages, which are not affected too much by such smoothing.

3. Asymmetry of tropical precipitation changes

Figure 1 shows seasonal variation of the global mean, tropical mean, and hemispherical mean of the precipitation anomalies from the multimodel ensemble. The global mean (90°S–90°N) and tropical mean (0°–30°) of the precipitation anomalies are obtained for each month, similar to the Southern (Northern) Hemispheric mean of the precipitation anomalies over the globe (0°–90°) and in the tropics (±30°). The months of August, September, and October (ASO) and February, March and April (FMA) are used because they give the greatest asymmetric response of hemispheric averaged precipitation changes: the former has maximum (minimum) averaged precipitation anomalies and the latter has minimum (maximum) anomalies for the Northern

(Southern) Hemisphere (Chou et al. 2007). In the late boreal summer (ASO), for hemispherical averages of the precipitation anomalies in the tropics, the northern average (0°–30°N) indicates strong positive trends, while the southern average (30°S–0°) shows weak negative trends (Fig. 1a). In the late austral summer (FMA), the trends are reversed (Fig. 1b). Hemispherical averages presented here look differently from those in Chou et al. (2007) because the latter removes the positive tropical mean but the former does not. This result implies a strong seasonal variation of hemispheric averaged tropical precipitation anomalies: a strong positive trend over the summer hemisphere and a weak negative trend over the winter hemisphere. Note that the entire tropical or global averages found no such asymmetry at all. A similar finding of the asymmetry is also seen for the hemispheric mean of precipitation anomalies averaged over the globe (0°–90°), but their amplitude is slightly smaller than those in the tropical averages. Moreover, the hemispheric mean of the precipitation anomalies over the winter hemisphere has a weak positive trend instead of a weak negative trend. This implies that the precipitation anomalies averaged over higher latitudes (30°–90°) of the summer and winter hemispheres are both positive (not shown), which has been discussed in recent studies (Meehl et al. 2007; Zhang et al. 2007). In other words, this precipitation asymmetry occurs only in the tropics (30°S–30°N). Thus, we will focus on tropical precipitation in the following analysis and discussion.

This precipitation asymmetry can be consistently seen in hemispheric averages of all 13 model simulations (Fig. 2). For departures from the tropical mean of the precipitation anomalies, all 13 model results show positive anomalies for the summer hemispheric averages and negative anomalies for the winter hemispheric
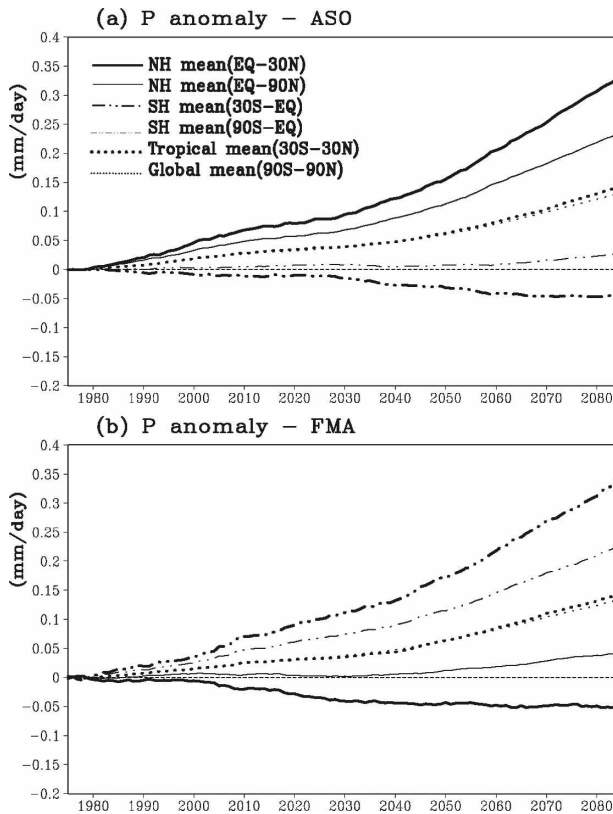
(a) P anomaly – ASO

(b) P anomaly – FMA

FIG. 1. Changes of precipitation departures (mm day^{-1}) from the 1961–90 averages for the multimodel ensemble in the SRES A2 global warming scenario in (a) ASO and (b) FMA. For the tropics Northern Hemisphere (0°–30°N, thick solid line), Southern Hemisphere (0°–30°S, thick dot–dot–dashed line), and tropical (30°S–30°N, thick dotted line) means; for the globe Northern Hemisphere (0°–90°N, thin solid line), Southern Hemisphere (0°–90°S, thin dot–dot–dashed line), and global (90°S–90°N, thin dotted line) means. The zero line is the thin dashed line; 30-yr running mean is used.

averages. Note that such asymmetry is found not only in the hemispheric difference but also in the seasonal precipitation range: the wet region (season) becomes wetter and the dry region (season) becomes slightly drier or remains unchanged. At the end of the twenty-first century in ASO, the Northern Hemispheric average of the tropical precipitation anomalies varies from 0.15 to 0.5 mm day^{-1} (−0.2 to 0.1 mm day^{-1} for the Southern Hemisphere); the change of the hemispheric difference is around 0.2–0.65 mm day^{-1} (4%–20% relative to the current climate of respective models). In FMA, on the other hand, the Southern Hemisphere average of the precipitation anomalies is from 0.1 to 0.6 mm day^{-1} (−0.2–0 mm day^{-1} for the Northern Hemisphere); the change of the hemispheric difference is around 0.15–0.8 mm day^{-1} (3%–24%). For both Northern and Southern Hemispheres, the change of the seasonal precipitation

range is around 0.1–0.7 mm day^{-1}. Compared to observations, such as in Chou et al. (2007), the observed seasonal precipitation range and hemispheric difference are larger than in model simulations. The discrepancy of the larger changes for the observation is consistent with Allan and Soden (2007), Wentz et al. (2007), and Zhang et al. (2007). For the multimodel ensemble, the change of the hemispheric difference is 0.4 mm day^{-1} (12%) in ASO and 0.45 mm day^{-1} (14%) in FMA; the change of the seasonal precipitation range is about 0.4 mm day^{-1} for both hemispheres. These values are much larger than the change of the averages of the entire tropics, so both the hemispheric difference and the seasonal precipitation range of the multimodel ensemble might be useful indicators for detecting global warming impacts on tropical precipitation.

To further examine the asymmetry of the precipitation anomalies, the seasonal variation of zonal-mean anomalies of the multimodel ensemble is shown in Fig. 3. The precipitation anomalies show a meridional movement with seasons, which roughly follows the seasonal migration of the climatological precipitation, denoted by a 4 mm day^{-1} contour of the climatological mean (thick solid line). The maximum zonal-mean precipitation anomalies of the multimodel ensemble are about 1 mm day^{-1} at 5°S in January–April. The negative precipitation anomalies are mainly distributed outside the main convective region. However, some relatively stronger negative precipitation anomalies are also found over the margin of convective regions, 5°–10°N during February–June. Overall, the negative precipitation anomalies can occur either in the subsidence regions or in the margin of convective regions.

Further examination of the spatial distribution for the multimodel ensemble precipitation and surface temperature anomalies is described in Fig. 4. Most positive rainfall anomalies occur in the summer hemisphere. The magnitude of positive precipitation anomalies is much greater than that of negative precipitation anomalies in both ASO and FMA. Moreover, the area of stronger positive precipitation anomalies (amplitude larger than 0.5 mm day^{-1}) is broader than that of stronger negative precipitation anomalies. Note that the positive precipitation anomaly regions in FMA are mainly located over oceanic regions, especially the Pacific and Indian Oceans, while those in ASO spread in oceanic regions as well as land areas, such as South Asia and Southeast Asia, which are dominated by the Asian summer monsoon. Moreover, positive precipitation anomalies are found to coincide well with the current-climate main convective regions, denoted in heavy solid lines. They imply a relationship between positive precipitation anomalies and current-climate main con-
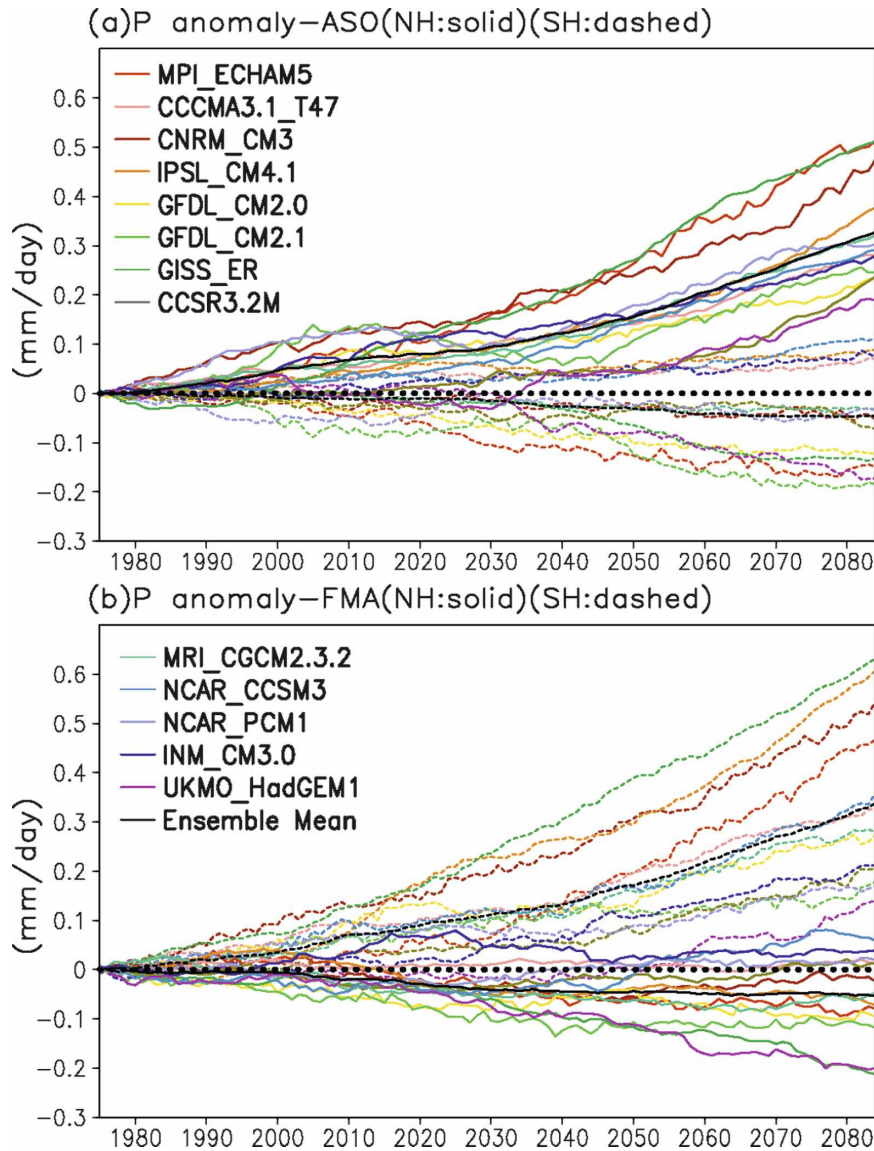
(a)P anomaly—ASO(NH:solid)(SH:dashed)

Legend:
- MPI_ECHAM5
- CCCMA3.1_T47
- CNRM_CM3
- IPSL_CM4.1
- GFDL_CM2.0
- GFDL_CM2.1
- GISS_ER
- CCSR3.2M

(b)P anomaly—FMA(NH:solid)(SH:dashed)

Legend:
- MRI_CGCM2.3.2
- NCAR_CCSM3
- NCAR_PCM1
- INM_CM3.0
- UKMO_HadGEM1
- Ensemble Mean

FIG. 2. As in Fig. 1 but for all 13 model simulations in (a) ASO and (b) FMA. Solid lines are for Northern Hemisphere (0°–30°N) and dashed lines are for Southern Hemisphere (0°–30°S) averages: ensemble mean (black curve) and zero line (thick dotted line) also plotted.

vection zones, which may be associated with the rich-get-richer mechanism (Chou and Neelin 2004). Maximum positive precipitation anomalies are about 1.5 mm day^{-1} in ASO and 2.5 mm day^{-1} in FMA. The drying regions with larger negative precipitation anomalies, over −0.5 mm day^{-1}, often occur next to positive precipitation anomaly regions. In the late boreal summer, strong drying occurs west of Indonesia and near the Caribbean Sea and Central America, which is over the margin of convective regions (Fig. 4a). The drying over the Caribbean Sea and Central America is consistent with the observation (Neelin et al. 2006). In late austral summer, two strong drying regions are found north and south of the equatorial eastern Pacific, where maximum precipitation anomalies are found (Fig. 4b). This pattern of the precipitation anomalies over the eastern Pacific implies an El Niño–like response. In examining the corresponding surface temperature distribution (shaded area of Fig. 4), we did find El Niño–like surface temperature anomalies, which often occur under global warming (Meehl and Washington 1996; Teng et al. 2006; Meehl et al. 2007). This El Niño–like pattern is more apparent in FMA than in ASO. The surface temperature anomalies are used in Fig. 4, instead of sea
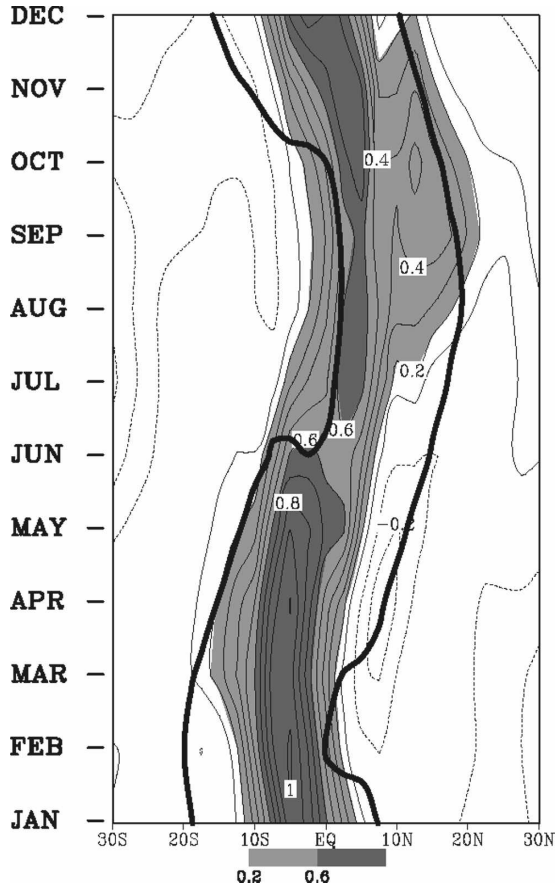
FIG. 3. Time–latitude domain of the zonal averages for the multimodel ensemble anomalies: differences of 2070–99 minus 1961–90 precipitation (mm day^{-1}). Heavy solid line is the 4 mm day^{-1} contour of the climatological precipitation in 1961–90.

surface temperature (SST) because the surface temperature data (in 13 models) is more complete than SST data (in 11 models) and both temperature anomalies are similar. The El Niño–like surface temperature (or SST) anomalies might be associated with the reduction of upwelling in the tropical east Pacific, which leads to warm SST anomalies (Vecchi and Soden 2007). It suggests that El Niño–like conditions might become permanent in a warmer world. We also note that there is no significant signal in the tropical Atlantic (Fig. 4), owing to the lack of robust anomalies among the climate model simulations.

Figure 4 shows strong spatial distribution of tropical precipitation anomalies, which could be dominated by large-scale features such as El Niño and the Asian summer monsoon. Thus, we are further examining the impacts of those large-scale features on the tropical precipitation asymmetry (Fig. 5). In FMA, the precipitation change over the eastern Pacific (180°–90°W) exhibits an asymmetry (red lines in Fig. 5b), consistent

with the previous studies (Chou and Lo 2007; Chou and Tu 2008): positive precipitation anomalies over the Southern Hemisphere and negative precipitation anomalies over the Northern Hemisphere. Its contribution to the precipitation asymmetry of the tropical averages (thick solid and thick dot–dot–dashed lines in Fig. 1b) is ~43%, but it does not affect the scattering of the asymmetry among climate models shown in Fig. 2b too much (not shown). In ASO, the precipitation over the Asian monsoon region (0°–30°N, 60°–150°E) is enhanced in every climate model (not shown), which has been discussed in various studies (e.g., Christensen et al. 2007; Kimoto 2005; Ueda et al. 2006), so the enhancement of the Asian summer monsoon rainfall also induces a tropical precipitation asymmetry (green lines in Fig. 5a). The Asian summer monsoon rainfall contributes ~42% to the precipitation asymmetry over the entire tropics (Fig. 1a), but it does not affect the scattering of the precipitation asymmetry shown in Fig. 2a (solid lines) too much (not shown).

4. Diagnosis of hemispheric precipitation anomalies

a. The moisture and moist static energy budget

The above analysis clearly presents robust responses of tropical precipitation asymmetry from a hemispheric point of view among the 13 model simulations that we used here. Since convection is the main process for inducing precipitation in the tropics, the vertically integrated moisture and moist static energy (MSE) equations are used to understand what dominant processes are affecting the asymmetric precipitation distribution.

Considering time or ensemble averages, the vertically integrated moisture equation can be written as

$$\langle \boldsymbol{\nabla} \cdot (\mathbf{v}q) \rangle = E - P, \tag{1}$$

where E is evaporation, $\mathbf{v}$ is horizontal velocity, and the specific humidity q is in energy units by absorbing the latent heat per unit mass L. The angle brackets denote a mass integration throughout the troposphere with p_T as the depth of the troposphere:

$$\langle X \rangle = \frac{1}{g} \int_{p_s}^{p_s - p_T} X \, dp, \tag{2}$$

where g is gravity and p_S is surface pressure. The precipitation is presented by energy unit W m^{-2}, which when divided by 28 is mm day^{-1}. Equation (1) is in a flux form: the divergence of moisture flux $\mathbf{v}q$ is balanced by moisture source (E) and sink (P). With the
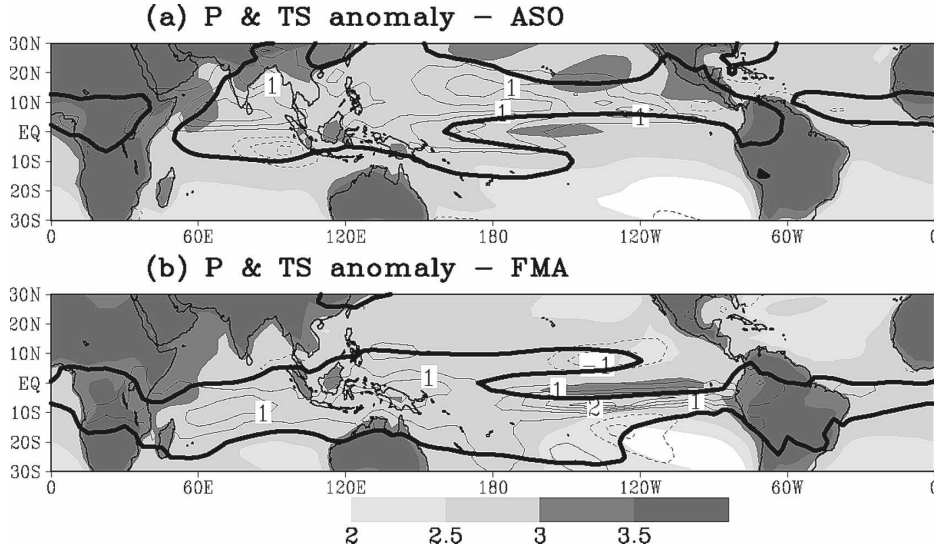
FIG. 4. Spatial distribution of the multimodel ensemble anomalies: differences of 2070–99 minus 1961–90 precipitation (mm day^{-1}, contour line) and surface temperature anomalies (K, shaded) in (a) ASO and (b) FMA. Heavy solid line is the 4 mm day^{-1} contour of the climatology for the current climate (1961–90).

assumption of $\omega \approx 0$ at the surface and tropopause, the divergence of moisture flux can be estimated by

$$\langle \boldsymbol{\nabla} \cdot (\mathbf{v}q) \rangle \approx \langle \mathbf{v} \cdot \boldsymbol{\nabla}q \rangle + \langle \omega \partial_p q \rangle, \quad (3)$$

where ω is pressure velocity. Thus, the precipitation anomalies induced by global warming can be estimated by

$$P' \approx -\langle \omega' \partial_p \overline{q} \rangle - \langle \overline{\omega} \partial_p q' \rangle - \langle \mathbf{v} \cdot \boldsymbol{\nabla}q \rangle' + E', \quad (4)$$

where the angle brackets with overbar denote the climatology of the current climate and angle brackets with prime represent the departure from the current climate climatology. The first term on the right of (4) $-\langle \omega' \partial_p \overline{q} \rangle$ is a dynamical feedback associated with the anomalous vertical motion. The second term on the rhs of (4) $-\langle \overline{\omega} \partial_p q' \rangle$ is associated with the vertical gradient of moisture anomalies, which is more associated with thermodynamic processes. Both "dynamic" and "thermodynamic" components are terminology used in Emori and Brown (2005) and Held and Soden (2006). The horizontal advection term $-\langle \mathbf{v} \cdot \boldsymbol{\nabla}q \rangle'$ is associated with anomalous horizontal moisture advection. Some nonlinear terms, such as $-\langle \omega' \partial_p q' \rangle$, are neglected from Eq. (6) owing to relatively small magnitudes.

To estimate the change of vertical velocity associated with the dynamical feedback in the moisture budget $-\langle \omega' \partial_p \overline{q} \rangle$, the anomalous vertically integrated MSE budget is used:

$$\langle \omega' \partial_p \overline{h} \rangle \approx -\langle \overline{\omega} \partial_p h' \rangle - \langle \mathbf{v} \cdot \boldsymbol{\nabla}(q + T) \rangle + F^{\text{net}\prime}, \quad (5)$$

where T is atmospheric temperature in energy units that absorbs the heat capacity at constant pressure Cp, and the MSE is $h = q + s$. The dry static energy is $s = T + \phi$, with ϕ being the geopotential. The net energy into the atmospheric column is

$$F^{\text{net}} = F_t - F_s. \quad (6)$$

The net heat flux at the top of the atmosphere (TOA) is

$$F_t = S_t^{\downarrow} - S_t^{\uparrow} - R_t^{\uparrow}, \quad (7)$$

and the net heat flux at the surface is

$$F_s = S_s^{\downarrow} - S_s^{\uparrow} - R_s^{\downarrow} - R_s^{\uparrow} - E - H, \quad (8)$$

with the assumption $R_t^{\downarrow} \approx 0$. Subscripts s and t on the solar ($S^{\downarrow}$ and $S^{\uparrow}$) and longwave ($R^{\downarrow}$ and $R^{\uparrow}$) radiative terms denote surface and model top, and H is sensible heat flux. Positive F_t and F_s indicate downward heat fluxes. In (5), the term associated with ω', that is, $\langle \omega' \partial_p \overline{h} \rangle$, is roughly balanced by anomalous vertical MSE transport associated with mean flow $-\langle \overline{\omega} \partial_p h' \rangle$, horizontal MSE transport anomalies $-\langle \mathbf{v} \cdot \boldsymbol{\nabla}(T + q) \rangle'$, and $F^{\text{net}\prime}$. The nonlinear and transient terms are also neglected here.

b. Diagnosis

The moisture budget for all 13 model simulations has been analyzed, but only the ensemble mean is shown. For simplicity, even though the partitioning of each
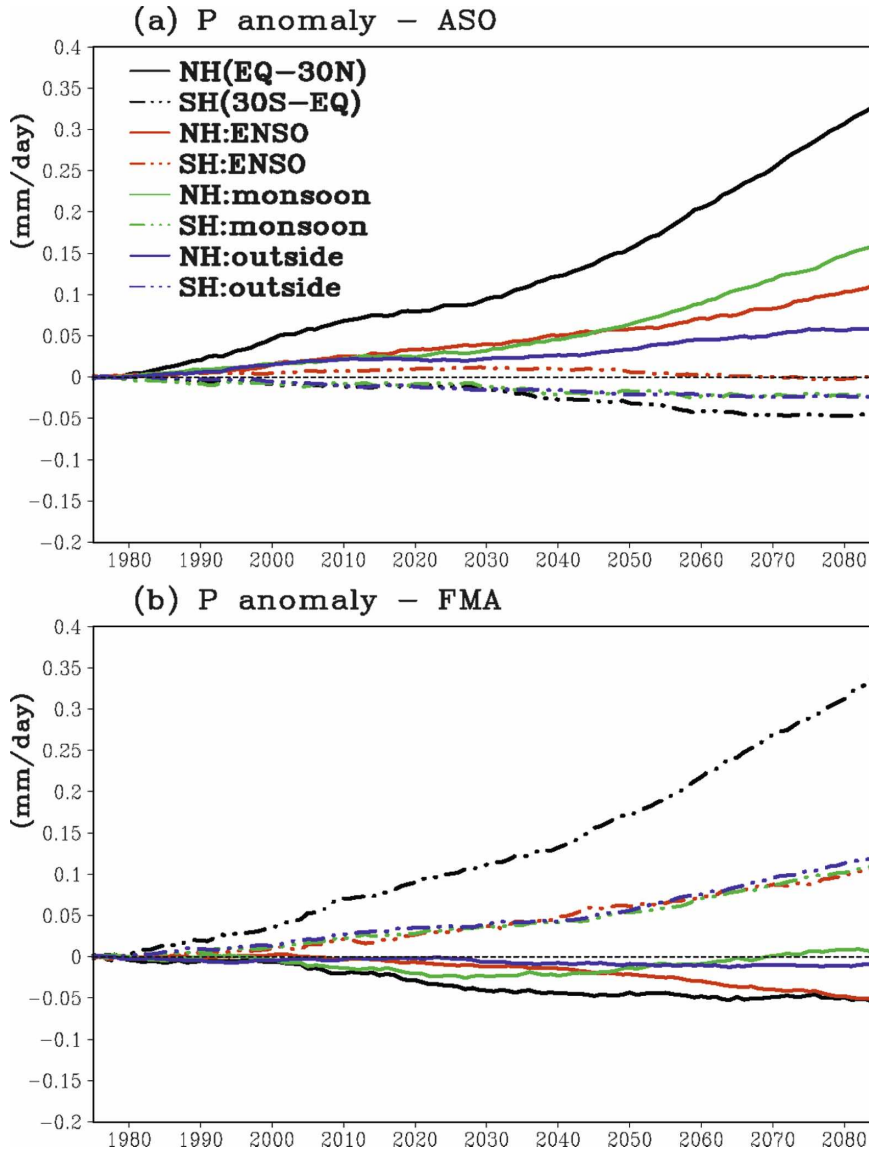
FIG. 5. As in Fig. 1 but for the Northern Hemisphere (0°–30°N, black solid line) and Southern Hemisphere (0°–30°S, black dot–dot–dashed line) means: averages over the ENSO region (red lines), the Asian monsoon region (green lines), and the area outside the ENSO and Asian monsoon regions (blue lines).

term in the moisture budget slightly differs among the model simulations, the ensemble mean can still capture a rough contribution of each term. Zonal averages for the years 2070–99 minus years 1961–90 from the multimodel ensemble in ASO and FMA are presented in Fig. 6. As in Fig. 1, an asymmetric pattern of the tropical precipitation anomalies with positive anomalies over the summer hemisphere and negative anomalies over the winter hemisphere is found. Most positive precipitation anomalies are much greater than negative precipitation anomalies. Maximum precipitation anomalies are clearly found at 5°N in ASO and at 5°S

in FMA, while no clear minimum is found. The maximum is around 0.7 mm day^{-1} in ASO and 1 mm day^{-1} in FMA. Similar meridional distributions of tropospheric moisture anomalies are found, but the meridional gradient of moisture anomalies is smoother and the moisture anomalies are all positive (Fig. 6b).

The meridional distribution of the thermodynamic term $-\langle \overline{\omega} \partial_p q' \rangle$ roughly resembles the skewed pattern of the precipitation anomalies: both maxima of the precipitation anomalies and $-\langle \overline{\omega} \partial_p q' \rangle$ are in the same hemisphere (Fig. 6c). The maximum $-\langle \overline{\omega} \partial_p q' \rangle$ is around 10°N in ASO and 10°S in FMA; thus, the maxi-
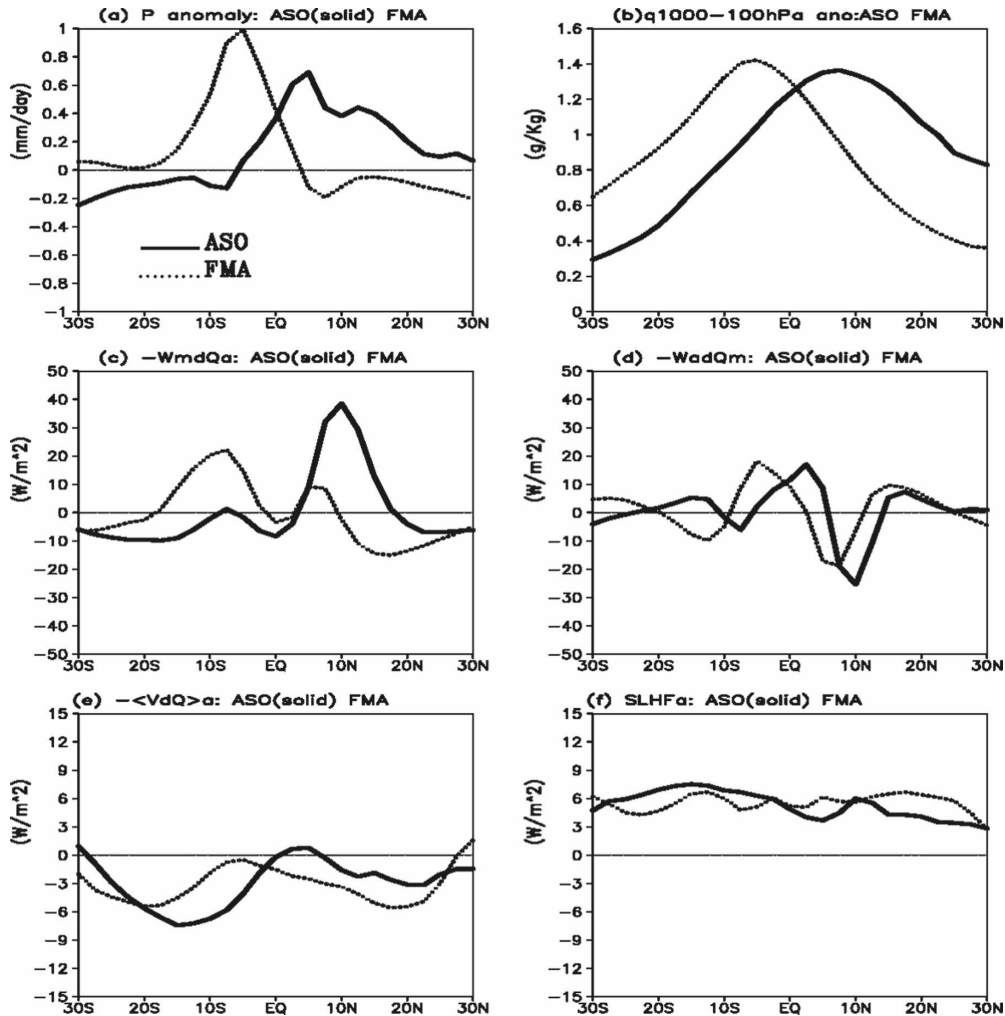
FIG. 6. Zonal averages of the moisture budget components of (a) precipitation anomalies (mm day^{-1}), (b) tropospheric moisture anomalies (g kg^{-1}); (c) $-\langle\overline{\omega}\partial_p q'\rangle$ in energy units (W m^{-2}), (d) $-\langle\omega'\partial_p\overline{q}\rangle$ (W m^{-2}), and (e) $-\langle\mathbf{v}\cdot\boldsymbol{\nabla}q\rangle'$ (W m^{-2}); and (f) evaporation anomalies (W m^{-2}) from the multimodel ensemble for ASO (solid lines) and FMA (dotted lines).

mum $-\langle\overline{\omega}\partial_p q'\rangle$ is a little more poleward than the maximum precipitation anomalies. A second peak is also found over the winter hemisphere (8°S in ASO and 8°N in FMA), which is associated with the common feature of a double intertropical convergence zone (ITCZ) that often occurs in climate models (Jungclaus et al. 2006). The amplitude of the maximum $-\langle\overline{\omega}\partial_p q'\rangle$ tends to be larger than that of the minimum $-\langle\overline{\omega}\partial_p q'\rangle$, especially in ASO. The maximum $-\langle\overline{\omega}\partial_p q'\rangle$ is 40 and 25 W m^{-2} in ASO and FMA, respectively. The minimum $-\langle\overline{\omega}\partial_p q'\rangle$, on the other hand, is -10 W m^{-2} in ASO and -15 W m^{-2} in FMA. This uneven amplitude of positive and negative anomalies is similar to the precipitation anomalies. Unlike $-\langle\overline{\omega}\partial_p q'\rangle$, the dynamical feedback $-\langle\omega'\partial_p\overline{q}\rangle$ has a very different distribution from the precipitation anomalies (Fig. 6d). In fact, $-\langle\omega'\partial_p\overline{q}\rangle$ tends

to have opposite signs of $-\langle\overline{\omega}\partial_p q'\rangle$ but with a little meridional shift. In other words, these two terms have a tendency to cancel each other out slightly. The amplitude of the maximum $-\langle\omega'\partial_p\overline{q}\rangle$ is roughly similar to that of the minimum $-\langle\omega'\partial_p\overline{q}\rangle$, with an amplitude of around ± 20 W m^{-2}. Compared to $-\langle\overline{\omega}\partial_p q'\rangle$, $-\langle\omega'\partial_p\overline{q}\rangle$ is slightly smaller in magnitude. However, at a regional scale, the magnitude of $-\langle\omega'\partial_p\overline{q}\rangle$ is larger than that of $-\langle\overline{\omega}\partial_p q'\rangle$, particularly in convective regions (Chou et al. 2006). It implies that a cancellation of the dynamical feedback occurs in zonal averages. The cancellation of the dynamical feedback becomes much stronger in hemispherical averages, so the magnitude of $-\langle\omega'\partial_p\overline{q}\rangle$ is much smaller than that of the thermodynamic component $-\langle\overline{\omega}\partial_p q'\rangle$ in hemispheric averages.

The horizontal moisture advection $-\langle\mathbf{v}\cdot\boldsymbol{\nabla}q\rangle'$ is also
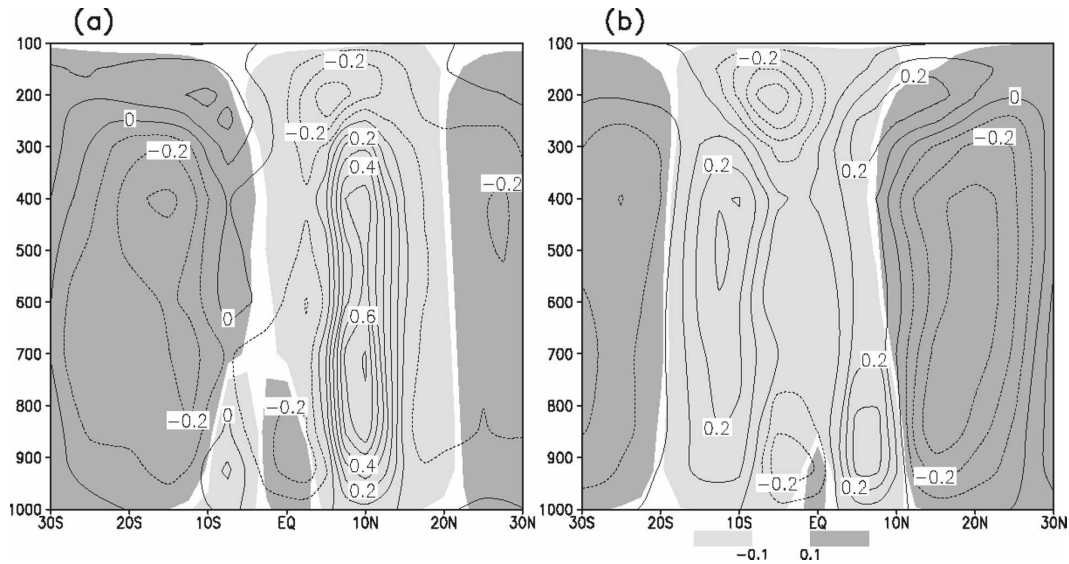
FIG. 7. The latitude–pressure domain of zonally averaged climatology in 1961–90 (shaded) and anomalies (contour) from the multimodel ensemble for (a) ASO and (b) FMA pressure velocity (Pa s^{-1} × 100).

shown in Fig. 6e. Anomalous dry advection, that is, $-\langle \mathbf{v} \cdot \nabla q \rangle' < 0$, prevails in most of the tropical regions. Near-zero or slightly positive $-\langle \mathbf{v} \cdot \nabla q \rangle'$ is found only for a small area around 5°N in ASO and 5°S in FMA, which coincides with maximum precipitation anomalies shown in Fig. 6a. In all three components of $-\langle \mathbf{v} \cdot \nabla q \rangle'$, the thermodynamic term $-\langle \overline{\mathbf{v}} \cdot \nabla q' \rangle$ is the most dominant term, while both the dynamical term $-\langle \mathbf{v}' \cdot \nabla \overline{q} \rangle$ and the nonlinear term $-\langle \mathbf{v}' \cdot \nabla q' \rangle$ are relatively small (not shown). Thus, mean inward flow ($\overline{\mathbf{v}}$) at the lower troposphere that is associated with the Hadley circulation tends to transport relatively dry air (smaller positive q' shown in Fig. 6b) from nonconvective to convective regions, so negative $-\langle \overline{\mathbf{v}} \cdot \nabla q' \rangle$ (or $-\langle \mathbf{v} \cdot \nabla q \rangle'$) is found to the north and south of the convective regions. The magnitude of $-\langle \mathbf{v} \cdot \nabla q \rangle'$ is from -9 to 1 W m^{-2} in ASO and -6 to 0 W m^{-2} in FMA. Similar to the moisture anomalies, the evaporation anomalies increase everywhere, with amplitude from 3 to 6 W m^{-2} (Fig. 6f). However, the evaporation anomalies are relatively uniform in latitude, with no clear meridional gradient. Overall, the thermodynamic term $-\langle \overline{\omega} \partial_p q' \rangle$ and the dynamical feedback $-\langle \omega' \partial_p \overline{q} \rangle$ are much larger than the evaporation anomalies and $-\langle \mathbf{v} \cdot \nabla q \rangle'$. However, from a hemispherical point of view, the thermodynamic term $-\langle \overline{\omega} \partial_p q' \rangle$ tends to be more asymmetric than the dynamical feedback $-\langle \omega' \partial_p \overline{q} \rangle$ owing to cancellation of similar amplitudes of positive and negative $-\langle \omega' \partial_p \overline{q} \rangle$.

The vertical gradients of mean moisture ($\overline{q}$) and moisture anomalies (q') are both positive and spatially uniform (Held and Soden 2006), so only mean vertical motion ($\overline{\omega}$) and vertical motion anomalies (ω') from the

model ensemble are analyzed to understand the variations of $-\langle \overline{\omega} \partial_p q' \rangle$ and $-\langle \omega' \partial_p \overline{q} \rangle$. The sign of the thermodynamic term $-\langle \overline{\omega} \partial_p q' \rangle$ depends on mean vertical motion ($\overline{\omega}$), which is associated with the mean Hadley circulation. The $-\langle \overline{\omega} \partial_p q' \rangle$ is positive over the ascending branch of the Hadley circulation and negative over the descending branch of the Hadley circulation. Thus, the distribution of $-\langle \overline{\omega} \partial_p q' \rangle$ in Fig. 6c is similar to the mean vertical motion ($\overline{\omega}$) in Figs. 7a and 7b (shaded). The sign of the dynamical feedback $-\langle \omega' \partial_p \overline{q} \rangle$ is mainly determined by anomalous vertical motion (ω') at a lower troposphere. In Fig. 6d, the distribution of $-\langle \omega' \partial_p \overline{q} \rangle$ implies a far more complicated pattern of anomalous vertical motion, particularly in the ascending regions, so a complicated distribution of the anomalous vertical motion can be expected. In ASO, an anomalous circulation of the same direction as the mean Hadley circulation is found in the inner side of the mean Hadley circulation (10°S–5°N), that is, anomalous ascent in mean ascent regions and anomalous descent in mean descent regions (Fig. 7a). However, over the outer side of the mean Hadley circulation, with mean ascent at 5°–20°N and mean descent south of 10°S, a reversed anomalous circulation is found, that is, anomalous descent in mean ascent regions and anomalous ascent in the mean descent regions. Similarly in FMA, the same direction of anomalous circulation is found over the inner side of the mean Hadley circulation (8°S–10°N). Over the outer side of the mean Hadley circulation, with mean ascent at 20°–8°S and mean descent north of 10°N, a reversed direction of anomalous circulation is found (Fig. 7b). Another notable feature is that two

local maxima of anomalous vertical motions are found at the lower troposphere around 800 hPa and in the upper troposphere around the level of 200 hPa in both ASO and FMA. The maxima in the upper troposphere might be due to the occurrence of tropopause lifting in a warmer climate (Holzer and Boer 2001; Santer et al. 2003; International Ad Hoc Detection and Attribution Group 2005). These two maxima of anomalous vertical motions should be further investigated. Considering the change of the entire Hadley circulation, Fig. 7 implies a weakening of the Hadley circulation, particularly over the descending areas, which has been discussed in various studies (Held and Soden 2006; Lu et al. 2007; Vecchi and Soden 2007).

We next examine the MSE budget (5) to understand processes that induce anomalous vertical velocity ω'. Unlike $-\langle\omega'\partial_p\overline{q}\rangle$ in Fig. 6d, which is mainly associated with the change of vertical velocity at a lower troposphere, $\langle\omega'\partial_p\overline{h}\rangle$ (Fig. 8a) is much more complicated because $\langle\omega'\partial_p\overline{h}\rangle$ is affected by ω' at every level. Since the MSE budget in FMA is similar to that in ASO, we only discuss the ASO budget here. Over the convergence zones that are mostly in the Northern Hemisphere, positive $\langle\omega'\partial_p\overline{h}\rangle$ occurs everywhere, with a maximum around 10°N, which coincides well with the precipitation anomalies shown in Fig. 6a. However, the two components of $\langle\omega'\partial_p\overline{h}\rangle$ ($\langle\omega'\partial_p\overline{s}\rangle$ and $\langle\omega'\partial_p\overline{q}\rangle$) are quite different from the distribution of $\langle\omega'\partial_p\overline{h}\rangle$, with a sign change around the areas near 10°N. Thus, we examine the MSE budget over the areas near 10°N and the areas outside the areas near 10°N separately. Outside the areas around 10°N, the anomalous vertical motion is upward (Fig. 7a), so $\langle\omega'\partial_p\overline{s}\rangle$ is positive and $\langle\omega'\partial_p\overline{q}\rangle$ is negative. The positive $\langle\omega'\partial_p\overline{h}\rangle$ over these areas is mainly contributed by positive $\langle\omega'\partial_p\overline{s}\rangle$ as the magnitude of negative $\langle\omega'\partial_p\overline{q}\rangle$ is smaller than that of positive $\langle\omega'\partial_p\overline{s}\rangle$. Examining the terms on the right of the MSE budget (5) for those regions, positive $-\langle\overline{\omega}\partial_p h'\rangle$ dominates most areas with maximum at 10°N (Fig. 8b), while positive $F^{net\prime}$ and $-\langle\mathbf{v}\cdot\mathbf{\nabla}(T+q)\rangle'$ dominate the areas near the equator (Figs. 8g and 8h). Positive $-\langle\overline{\omega}\partial_p h'\rangle$ implies a reduction of effective static stability, which has been termed as the rich-get-richer mechanism (Chou and Neelin 2004; Chou et al. 2006). Positive $F^{net\prime}$ is associated with ocean dynamical feedbacks via surface heat flux exchange (Chou et al. 2006).

Around the areas near 10°N, on the other hand, the MSE budget is very different even though $\langle\omega'\partial_p\overline{h}\rangle$ is also positive. First, $\langle\omega'\partial_p\overline{s}\rangle$ is negative and $\langle\omega'\partial_p\overline{q}\rangle$ is positive, a reversal to the areas outside the regions near 10°N. This indicates anomalous downward motion. The magnitude of negative $\langle\omega'\partial_p\overline{s}\rangle$ is smaller than that of positive $\langle\omega'\partial_p\overline{q}\rangle$, so $\langle\omega'\partial_p\overline{h}\rangle$ is positive. The relatively

small magnitude of $\langle\omega'\partial_p\overline{s}\rangle$ is contributed by enhanced upward velocity anomalies above 250 hPa (Fig. 7a). Thus, the downward velocity anomalies occur only at the middle and lower troposphere, while the upward velocity anomalies dominate upper troposphere. This vertical structure of the anomalous vertical motion implies an uplift of convection, which has been discussed in detail in Chou et al. (2008, manuscript submitted to *J. Climate*, hereafter C08). Interestingly, the maximum $-\langle\overline{\omega}\partial_p q'\rangle$ and minimum $-\langle\overline{\omega}\partial_p s'\rangle$, which imply a convective center with maximum upward motion, are also found around 10°N (Figs. 8d and 8f). This implies that deepening of convection could be associated with an uplift of the tropopause in a warmer climate.

The ascending area around 8°S is also noteworthy, which is associated with anomalous downward motion. Unlike the positive precipitation anomalies over the areas near 10°N, the precipitation anomalies over this region are negative. The corresponding downward velocity anomalies are found throughout the entire troposphere, which is also different from those over the areas near 10°N (Fig. 7a). Examining the MSE budget (5), the anomalous downward motion and the negative precipitation anomalies are associated with negative $-\langle\mathbf{v}\cdot\mathbf{\nabla}(T+q)\rangle'$, consistent with the upped-ante mechanism (Chou and Neelin 2004; Chou et al. 2006).

Over the descending regions, such as the Southern Hemisphere, the corresponding tropical circulation could be determined by other processes such as the balance of the adiabatic forcing and the longwave radiation, so the MSE budget might not be appropriate to diagnose the change of the circulation. Over these regions, the mean downward velocity is reduced (Fig. 7a) over the areas between 10° and 20°S but enhanced over the areas south of 20°S (Fig. 7a). Considering the areas between 10° and 20°S first, the anomalous upward velocity could be associated with positive $F^{net\prime}$ (Fig. 8h). Further examining of the vertical profile of the anomalous vertical motion, the upward velocity anomalies, which indicate a reduction of mean downward motion, occur only in middle and lower troposphere, while downward velocity anomalies, which indicate an enhancement of mean downward velocity, are found above 250 hPa. This implies a deepening of subsidence that is a counterpart of the tropical circulation associated with the deepening of the convection around 10°N. Thus, the descending motion is reduced. Over these descending regions, the dynamical feedback associated with $-\langle\omega'\partial_p\overline{q}\rangle$ tends to increase precipitation. However, the thermodynamic component associated with $-\langle\overline{\omega}\partial_p q'\rangle$ is more dominant (Figs. 6c and 6d), so precipitation is actually reduced. Over the areas south of
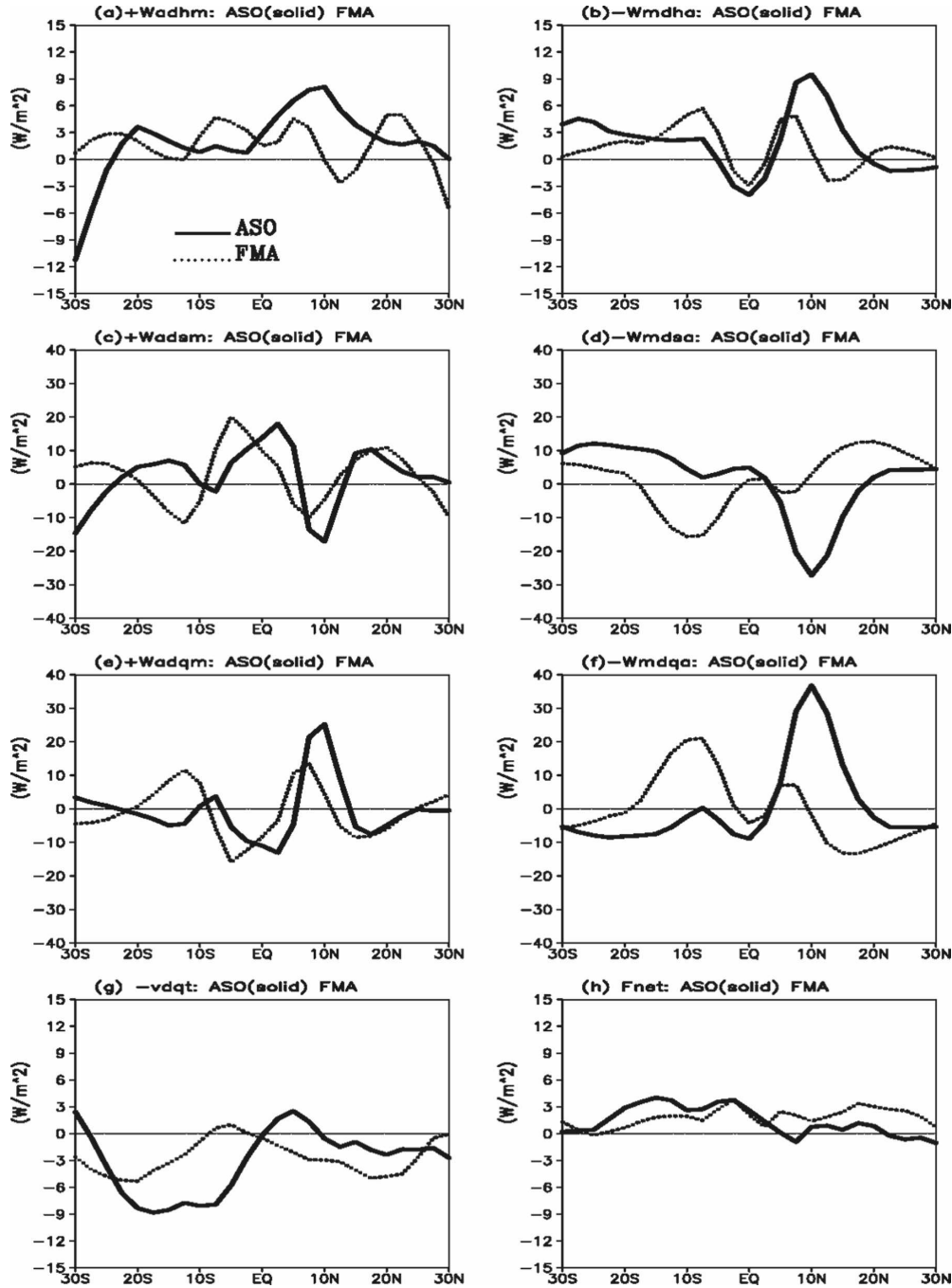
FIG. 8. Zonal averages of the MSE budget components (a) $\langle \omega' \partial_p \overline{h} \rangle$, (b) $-\langle \overline{\omega} \partial_p h' \rangle$, (c) $\langle \omega' \partial_p \overline{s} \rangle$, (d) $-\langle \overline{\omega} \partial_p s' \rangle$, (e) $\langle \omega' \partial_p \overline{q} \rangle$, (f) $-\langle \overline{\omega} \partial_p q' \rangle$, (g) $-\langle \mathbf{v} \cdot \nabla (T + q) \rangle'$, and (h) $F^{\mathrm{net}\prime}$ anomalies from the multimodel ensemble for ASO (solid lines) and FMA (dotted lines): All variables in energy units (W m^{-2}).

20°S, on the other hand, the mean descending motion is strengthened owing to stronger longwave radiation cooling (not shown). Thus, both dynamical and thermodynamic effects tend to reduce precipitation (Figs. 6c and 6d). A more detailed discussion can be found in C08.

5. The robustness of tropical precipitation anomalies

The distribution of zonal-mean precipitation anomalies for all 13 model simulations in ASO and FMA is presented in Fig. 9. Hemispherically, all 13 model simu-
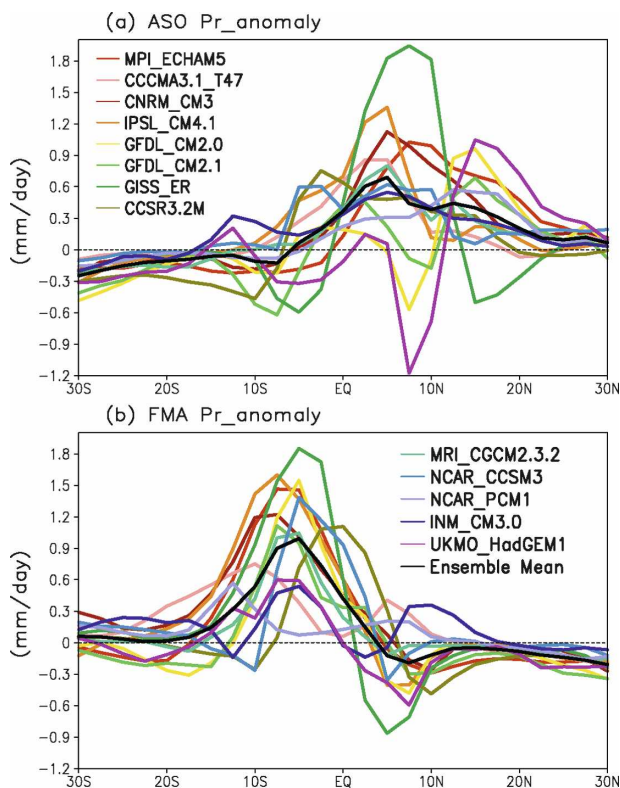
FIG. 9. Zonal averages of precipitation anomalies (mm day^{-1}) for all 13 climate models (contour types noted in legend) in (a) ASO and (b) FMA.

FIG. 10. As in Fig. 9 but for $-\langle \overline{\omega}\partial_p q' \rangle$ (W m^{-2}).

lations are consistent, with maximum precipitation anomalies over the Northern (Southern) Hemisphere in the boreal (austral) summer and negative precipitation anomalies over the other side of the equator. Zonally, on the other hand, the distribution becomes much more scattered. The distribution of zonal-mean precipitation anomalies are more scattered in the boreal summer (Fig. 9a) than in austral summer (Fig. 9b); this is mostly caused by three model simulations, GFDL CM2.0, GISS-ER, and UKMO HadGEM1. The poleward migration of the major rainband is usually associated with summer monsoon systems, which is induced by the meridional temperature gradient associated with land–sea heating contrast (e.g., Li and Yanai 1996; Chou 2003). Thus, the greater scattering of the boreal summer precipitation anomalies implies that changes of the Asian summer monsoon systems under global warming might be different among climate model simulations. Examining the contribution of the Asian summer monsoon rainfall, it does create some scattering in the meridional distribution of the zonal mean of the precipitation anomalies, particularly in GFDL CM2.0, GISS-ER, and UKMO HadGEM1. Overall, a robustness of tropical precipitation changes is found for all 13
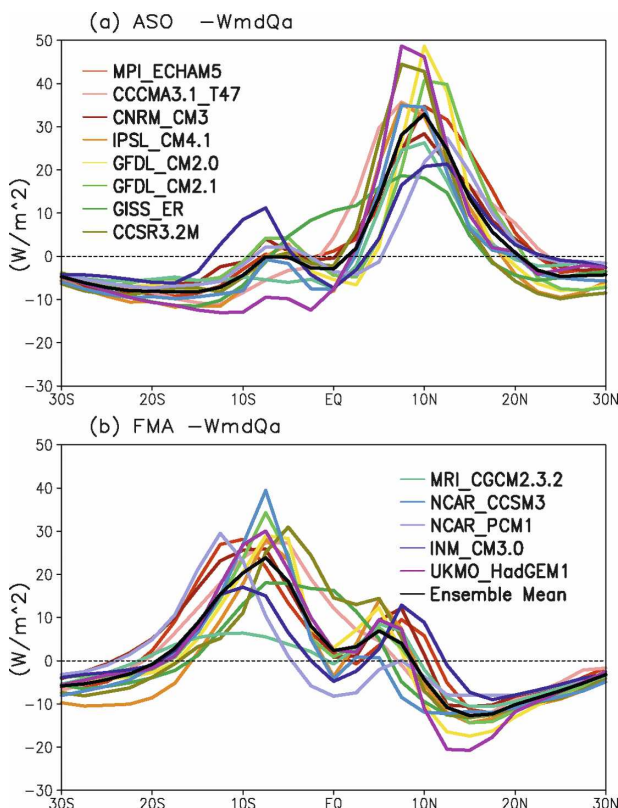
climate model simulations: maximum anomalies over the summer hemisphere and slightly negative anomalies over the winter hemisphere.

We next examine 13 model simulations for the zonal-mean distribution of $-\langle \overline{\omega}\partial_p q' \rangle$ and $-\langle \omega'\partial_p\overline{q} \rangle$. Figure 10 shows the zonal-mean distribution of $-\langle \overline{\omega}\partial_p q' \rangle$ for all 13 model simulations in ASO and FMA. The distribution of $-\langle \overline{\omega}\partial_p q' \rangle$ is very similar among the climate model simulations. Maximum $-\langle \overline{\omega}\partial_p q' \rangle$ occurs over the Northern Hemisphere in ASO and over the Southern Hemisphere in FMA for all 13 model simulations. Negative $-\langle \overline{\omega}\partial_p q' \rangle$ is also found over most of the other side of the equator, the Southern Hemisphere in ASO and the Northern Hemisphere in FMA. Unlike $-\langle \overline{\omega}\partial_p q' \rangle$, the distribution of $-\langle \omega'\partial_p\overline{q} \rangle$ is relatively inconsistent among the climate model simulations, particularly in ASO (Fig. 11). However, a "flying bird"–like pattern— positive anomalies in the center with negative anomalies at the north and south of this positive anomaly region—is consistently found close to the equatorial region (15°S–15°N) in most model simulations. This flying-bird pattern is particularly clear in FMA. From a hemispheric point of view, $-\langle \omega'\partial_p\overline{q} \rangle$ is much less asymmetric to the equator than $-\langle \overline{\omega}\partial_p q' \rangle$ mainly due to the cancellation of positive and negative anomalies on the
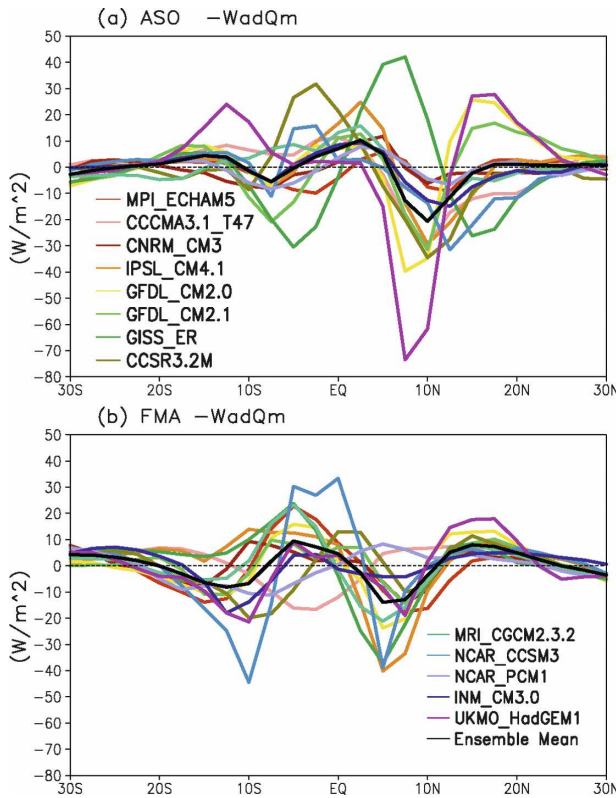
FIG. 11. As in Fig. 9 but for $-\langle\omega'\partial_p\overline{q}\rangle$ (W m^{-2}).

same side of the equator. The cancellation is consistently found among climate models. Thus, the asymmetry of the tropical precipitation anomalies is mainly caused by $-\langle\overline{\omega}\partial_p q'\rangle$, while $-\langle\omega'\partial_p\overline{q}\rangle$ is responsible for the scattering of the zonally averaged tropical precipitation anomalies shown in Fig. 9.

The robustness of the $-\langle\overline{\omega}\partial_p q'\rangle$ distribution implies that $\overline{\omega}$ associated with the Hadley circulation should be well simulated by climate models, and the moisture anomalies induced by global warming are similar among model simulations. Figures 11a and 11b show that the tropospheric moisture anomalies, indeed, have similar distributions among all 13 model simulations, with slight differences in magnitude. Held and Soden (2006) have suggested that climate models roughly obey the Clausius–Clapeyron equation, so the column-integrated water vapor increases as the globe warms up. Such moisture increase concentrates in the lower troposphere, and moisture increases more in convective than in nonconvective regions (not shown). All 13 models indicate that maximum moisture anomalies occur in the summer hemisphere. The zonal-mean vertical velocity at 500 hPa is used to represent the Hadley circulation. The distribution of the zonal-mean vertical velocity is very similar among the model simulations

(Figs. 12c and 12d), so the Hadley circulation is well simulated by the climate models. In conclusion, the consistent mean Hadley circulation and moisture anomalies create a similar $-\langle\overline{\omega}\partial_p q'\rangle$ distribution in all 13 CGCM simulations.

The distribution of the dynamical component $-\langle\omega'\partial_p\overline{q}\rangle$ is more similar to ω' than the vertical gradient of moisture $\partial_p\overline{q}$ since $\partial_p\overline{q} > 0$ is found everywhere and the distribution of $\partial_p\overline{q}$ is relatively smooth in space. In addition, $\partial_p\overline{q}$ is consistently well simulated by climate models (not shown). Thus, the scattering of $-\langle\omega'\partial_p\overline{q}\rangle$ shown in Fig. 10a is mainly due to the zonal mean of anomalous vertical motion. As the distribution of $-\langle\omega'\partial_p\overline{q}\rangle$ is much more scattered in the northern summer than in the southern summer, the northern summer monsoon systems associated with a strong land–sea heating contrast might be a possible cause for such inconsistency in the zonal averages of $-\langle\omega'\partial_p\overline{q}\rangle$ between the model simulations (e.g., Christensen et al. 2007; Kimoto 2005). This issue is worth further investigation and will be examined in the future.

The last term in the moisture budget equation, the horizontal moisture advection anomaly $-\langle\mathbf{v}\cdot\nabla q\rangle'$, is also analyzed (Fig. 13). The horizontal advection term $-\langle\mathbf{v}\cdot\nabla q\rangle'$ is relatively smaller than the thermodynamic term $-\langle\overline{\omega}\partial_p q'\rangle$ and the dynamical component $-\langle\omega'\partial_p\overline{q}\rangle$. The meridional distribution of $-\langle\mathbf{v}\cdot\nabla q\rangle'$ is relatively robust among all 13 climate model simulations, especially over the Southern Hemisphere. Most $-\langle\mathbf{v}\cdot\nabla q\rangle'$ is negative in the tropics and only positive $-\langle\mathbf{v}\cdot\nabla q\rangle'$ is found over the equatorial side of the main convection zone, around 5°N in ASO and 5°S in FMA, so dry advection anomalies prevail in most of the tropical regions. Examining three components of $-\langle\mathbf{v}\cdot\nabla q\rangle'$, $-\langle\mathbf{v}\cdot\nabla q\rangle'$ is the dominant term (not shown). This implies that the dry advection associated with the mean Hadley circulation dominates; that is, $-\langle\mathbf{v}\cdot\nabla q\rangle' < 0$. The mean circulation transfers relatively dry air from nonconvective regions to convective regions, which suppresses convection over the margins of mean ascending regions via the processes discussed in the MSE budget. Thus, this dry advection might be the cause of the flying-bird pattern in the distribution of $-\langle\omega'\partial_p\overline{q}\rangle$.

6. Conclusions

Thirteen CGCM model simulations for the SRES A2 warming scenario are used to study the robustness of tropical precipitation changes and the associated processes under global warming. The major findings in this study are:
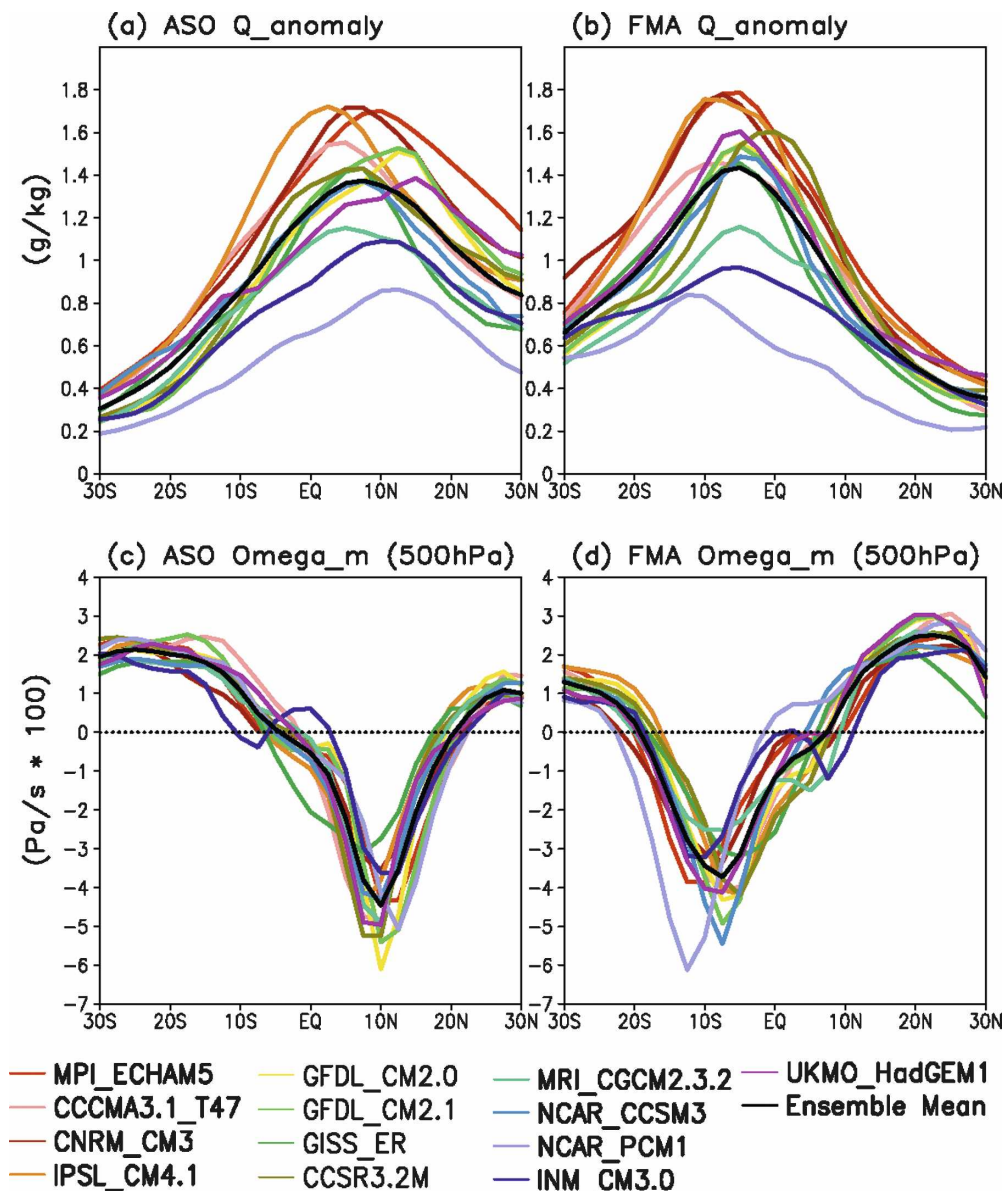
FIG. 12. As in Fig. 9 but for (a)–(b) the tropospheric moisture anomalies (g kg^{-1}) and (c)–(d) the climatological pressure velocity (Pa s^{-1} × 100) at 500 hPa in 1961–90.

1) The trends of the hemispherically averaged tropical precipitation vary strongly with season, which indicates an enhancement of the seasonal precipitation range, defined as differences between wet and dry seasons, and the hemispherical difference, defined as differences between summer and winter hemispheres.

2) The vertical moisture transport associated with the mean Hadley circulation is asymmetric to the equator, which is a robust feature among the 13 climate models and a major process for inducing the tropical precipitation asymmetry.

Considering averages in different seasons and over different hemispheres, the hemispheric-averaged tropical precipitation anomalies exhibit a robust asymmetric pattern among climate models: increased precipitation over the summer hemisphere and slightly reduced precipitation over the winter hemisphere. The change of the precipitation over the summer hemisphere is from 0.1 to 0.8 mm day^{-1} at the end of the twenty-first century, while the precipitation change over the winter hemisphere is from -0.2 to 0.1 mm day^{-1}. These are similar to those trends found in tropical ascend and descend regions (Table 2 in Allan and Soden 2007). For
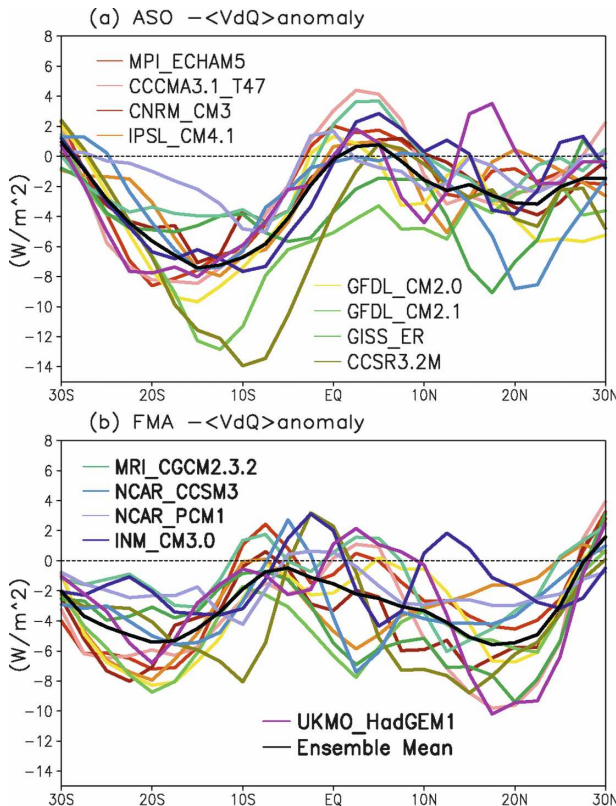
FIG. 13. As in Fig. 9 but for $-\langle \mathbf{v} \cdot \nabla q \rangle'$ (W m^{-2}).

the multimodel ensemble, the seasonal precipitation range is increased by about 12% relative to the current climate (0.4 mm day^{-1}) and the hemispheric difference is increased by about 14% (0.45 mm day^{-1}). These values are much larger than the change of the averages over the entire tropics (3% and 0.1 mm day^{-1}), so both the hemispheric difference and the seasonal precipitation range might be useful indicators for detecting global warming impacts on tropical precipitation. These changes in the climate model simulations are smaller than those in observations (Chou et al. 2007). This discrepancy has been discussed in several studies (Allan and Soden 2007; Wentz et al. 2007; Zhang et al. 2007). Examining the spatial distribution of the precipitation anomalies, the magnitude and area of positive precipitation anomalies are much greater and wider than those of negative precipitation anomalies in both ASO and FMA. Most positive precipitation anomalies are found in the convergence zones, while negative precipitation anomalies are found in the convective margins and the descending regions.

Based on the analysis of the vertically integrated moisture and MSE budgets, the thermodynamic component $-\langle \overline{\omega} \partial_p q' \rangle$ and the dynamical feedback $-\langle \omega' \partial_p \overline{q} \rangle$ were two relatively large terms that affect tropical pre-

cipitation. The thermodynamic component is associated with the mean Hadley circulation and the atmospheric moisture changes, which are well simulated in all 13 CGCM model simulations. The dynamical feedback, on the other hand, is much more complicated and inconsistent among climate models because it involves changes of tropical convergence and the corresponding circulation. However, from a hemispheric point of view, the thermodynamic term tends to be more asymmetric than the dynamical feedback owing to the cancellation of similar positive and negative dynamical amplitudes. Thus, the tropical precipitation asymmetry dominated by the thermodynamic component becomes a robust feature among climate models.

Under global warming, the change of the Hadley circulation is complicated. The anomalous circulation has the same (opposite) direction as the mean Hadley circulation in the inner (outer) side of the mean Hadley circulation. Considering the whole circulation, the Hadley circulation tends to be weakened in a warmer climate, which is particularly clear over the descending regions. Although the dynamical feedback does not play a crucial role in determining the asymmetry of tropical precipitation anomalies, possible mechanisms that induce the anomalous vertical velocity are examined here. Over the convergence zones, the "rich-get-richer" mechanism that is associated with a reduction of effective static stability induces upward velocity anomalies. Both deepening of the Hadley circulation and the "upped-ante" mechanism associated with dry advection induce downward velocity anomalies. Over the subsidence regions, on the other hand, the reduced mean downward velocity (upward velocity anomalies) is associated with positive anomalies of net energy into the atmosphere and deepening of the Hadley circulation.

REFERENCES

Allan, R. P., and B. J. Soden, 2007: Large discrepancy between observed and simulated precipitation trends in the ascending

and descending branches of the tropical circulation. *Geophys. Res. Lett.,* **34,** L18705, doi:10.1029/2007GL031460.

Allen, M. R., and W. J. Ingram, 2002: Constraints on future changes in climate and the hydrologic cycle. *Nature,* **419,** 224–232.

Boer, G. J., G. Flato, and D. A. Ramsden, 2000: A transient climate change simulation with greenhouse gas and aerosol forcing: Projected climate to the twenty-first century. *Climate Dyn.,* **16,** 427–450.

Chiang, J. C. H., and A. H. Sobel, 2002: Tropical tropospheric temperature variations caused by ENSO and their influence on the remote tropical climate. *J. Climate,* **15,** 2616–2631.

Chou, C., 2003: Land-sea heating contrast in an idealized Asian summer monsoon. *Climate Dyn.,* **21,** 11–25.

——, and J. D. Neelin, 2004: Mechanisms of global warming impacts on regional tropical precipitation. *J. Climate,* **17,** 2688–2701.

——, and M.-H. Lo, 2007: Asymmetric responses of tropical precipitation during ENSO. *J. Climate,* **20,** 3411–3433.

——, and J.-Y. Tu, 2008: Hemispherical asymmetry of tropical precipitation in ECHAM5/MPI-OM during El Niño and under global warming. *J. Climate,* **21,** 1309–1332.

——, J. D. Neelin, J.-Y. Tu, and C.-T. Chen, 2006: Regional tropical precipitation change mechanisms in ECHAM4/OPYC3 under global warming. *J. Climate,* **19,** 4207–4223.

——, J.-Y. Tu, and P.-H. Tan, 2007: Asymmetry of tropical precipitation change under global warming. *Geophys. Res. Lett.,* **34,** L17708, doi:10.1029/2007GL030327.

Christensen, J. H., and Coauthors, 2007: Regional climate projections. *Climate Change 2007: The Physical Science Basis,* S. Solomon et al., Eds., Cambridge University Press, 847–940.

Cubasch, V., and Coauthors, 2001: Projection of future climate change. *Climate Change 2001: The Science of Climate Change,* H. Houghton et al., Eds., Cambridge University Press, 527–582.

Dai, T., 2006: Precipitation characteristics in eighteen coupled climate models. *J. Climate,* **19,** 4605–4630.

——, M. L. Wigley, B. A. Boville, J. T. Kiehl, and L. E. Buja, 2001: Climates of the twentieth and twenty-first centuries simulated by the NCAR climate system model. *J. Climate,* **14,** 485–519.

Douville, H., F. Chauvin, S. Planton, J.-F. Royer, D. Salas-Mélia, and S. Tyteca, 2002: Sensitivity of the hydrological cycle to increasing amounts of greenhouse gases and aerosol. *Climate Dyn.,* **20,** 45–68.

Emori, S., and S. J. Brown, 2005: Dynamic and thermodynamic changes in mean and extreme precipitation under changed climate. *Geophys. Res. Lett.,* **32,** L17706, doi:10.1029/2005GL023272.

Fu, Q., C. M. Johanson, S. G. Warren, and D. J. Seldel, 2004: Contribution of stratospheric cooling to satellite-inferred tropospheric temperature trends. *Nature,* **429,** 55–58.

Held, I. M., and B. J. Soden, 2006: Robust responses of the hydrological cycle to global warming. *J. Climate,* **19,** 5686–5699.

Holzer, M., and G. J. Boer, 2001: Simulated changes in atmospheric transport climate. *J. Climate,* **14,** 4398–4420.

International Ad Hoc Detection and Attribution Group, 2005: Detection and attributing external influences on the climate system: A review of recent advances. *J. Climate,* **18,** 1291–1314.

Johns, T. C., and Coauthors, 2006: The new Hadley Centre climate model (HadGEM1): Evaluation of coupled simulations. *J. Climate,* **19,** 1327–1353.

Jones, P. D., and A. Moberg, 2003: Hemispheric and large-scale surface air temperature variations: An extensive revision and an update to 2001. *J. Climate,* **16,** 206–223.

Jungclaus, J. H., and Coauthors, 2006: Ocean circulation and tropical variability in the coupled model ECHAM5/MPI-OM. *J. Climate,* **19,** 3952–3972.

Karl, T. R., and K. E. Trenberth, 2003: Modern global climate change. *Science,* **302,** 1719–1723.

Kimoto, M., 2005: Simulated change of the east Asian circulation under global warming scenario. *Geophys. Res. Lett.,* **32,** L16701, doi:10.1029/2005GL023383.

Li, C., and M. Yanai, 1996: The onset and interannual variability of the Asian summer monsoon in relation to land–sea thermal contrast. *J. Climate,* **9,** 358–375.

Lu, J., G. A. Vecchi, and T. Reichler, 2007: Expansion of the Hadley cell under global warming. *Geophys. Res. Lett.,* **34,** L06805, doi:10.1029/2006GL028443.

Meehl, G. A., and W. M. Washington, 1996: El Niño–like climate change in a model with increased atmospheric CO_2 concentrations. *Nature,* **382,** 56–60.

——, W. D. Collins, B. A. Boville, J. T. Kiehl, T. M. L. Wigley, and J. M. Arblaster, 2000: Response of the NCAR climate system model to increased CO_2 and the role of physical processes. *J. Climate,* **13,** 1879–1898.

——, F. Zwiers, W. D. Collins, J. M. Arblaster, A. Hu, L. E. Buja, W. G. Strand, and H. Teng, 2005: How much more global warming and sea level rise? *Science,* **307,** 1769–1772.

——, and Coauthors, 2007: Global climate projection. *Climate Change 2007: The Physical Science Basis,* S. Solomon et al., Eds., Cambridge University Press, 747–845.

Mitchell, J. F. B., and Coauthors, 2001: Detection of climate change and attribution of causes. *Climate Change 2001: The Scientific Basis,* J. T. Houghton et al., Eds., Cambridge University Press, 695–738.

Neelin, J. D., and H. Su, 2005: Moist teleconnection mechanisms for the tropical South American and Atlantic sector. *J. Climate,* **18,** 3928–3950.

——, C. Chou, and H. Su, 2003: Tropical drought regions in global warming and El Niño teleconnections. *Geophys. Res. Lett.,* **30,** 2275, doi:10.1029/2003GL018625.

——, M. Munnich, H. Su, J. E. Meyerson, and C. E. Holloway, 2006: Tropical drying trends in global warming models and observations. *Proc. Natl. Acad. Sci. USA,* **103,** 6110–6115.

Roeckner, E., L. Bengtsson, J. Feichter, J. Lelieveld, and H. Rodhe, 1999: Transient climate change simulation with a coupled atmosphere–ocean GCM including the tropospheric sulfur cycle. *J. Climate,* **12,** 3004–3032.

Santer, B. D., and Coauthors, 1996: Human effect on global climate? *Nature,* **384,** 522–525.

——, and Coauthors, 2003: Contributions of anthropogenic and natural forcing to recent tropopause height changes. *Science,* **301,** 479–483.

——, and Coauthors, 2005: Amplification of surface temperature trends and variability in the tropical atmosphere. *Science,* **309,** 1551–1556.

Senior, C. A., and J. F. B. Mitchell, 2000: The time dependence of climate sensitivity. *Geophys. Res. Lett.,* **27,** 2686–2688.

Stott, P. A., J. F. B. Mitchell, J. M. Gregory, B. D. Santer, G. A. Meehl, and T. L. Delworth, 2006: Observational constraints on past attributable warming and predictions of future global warming. *J. Climate,* **19,** 3055–3069.

Teng, H., L. E. Buja, and G. A. Meehl, 2006: Twenty-first-century climate change commitment from a multi-model ensemble. *Geophys. Res. Lett.,* **33,** L07706, doi:10.1029/2005GL024766.

Tett, S. F. B., P. Stott, M. R. Allen, W. J. Ingram, and J. F. B. Mitchell, 1999: Causes of twentieth-century temperature change near the Earth's surface. *Nature,* **399,** 569–572.

——, and Coauthors, 2002: Estimation of natural and anthropogenic contributions to twentieth century temperature change. *J. Geophys. Res.,* **107,** 4306, doi:10.1029/2000JD000028.

Trenberth, K. E., and A. Dai, 2007: Effects of Mount Pinatubo volcanic eruption on the hydrological cycle as an analog of geoengineering. *Geophys. Res. Lett.,* **34,** L15702, doi:10.1029/2007GL030524.

——, and Coauthors, 2007: Observations: Surface and atmospheric climate change. *Climate Change 2007: The Physical Science Basis,* S. Solomon et al., Eds., Cambridge University Press, 235–336.

Ueda, H., A. Iwai, K. Kuwako, and M. E. Hori, 2006: Impact of anthropogenic forcing on the Asian summer monsoon as simulated by eight GCMs. *Geophys. Res. Lett.,* **33,** L06703, doi:10.1029/2005GL025336.

Vecchi, G. A., and B. J. Soden, 2007: Global warming and the weakening of the tropical circulation. *J. Climate,* **20,** 4316–4340.

Wentz, F. J., L. Ricciardulli, K. Hilburn, and C. Mears, 2007: How much more rain will global warming bring? *Science,* **317,** 233–235.

Williams, K. D., C. A. Senior, and J. F. B. Mitchell, 2001: Transient climate change in the Hadley Centre models: The role of physical processes. *J. Climate,* **14,** 2659–2674.

Zhang, X., F. W. Zwiers, G. C. Hegerl, F. H. Lambert, N. P. Gillett, S. Solomon, P. A. Scott, and T. Nozawa, 2007: Detection of human influence on twentieth-century precipitation trends. *Nature,* **448,** 461–465.